IEEE Access
Multidisciplinary ⋮ Rapid Review ⋮ Open Access Journal

Received 28 April 2024, accepted 9 May 2024, date of publication 14 May 2024, date of current version 21 May 2024.

Digital Object Identifier 10.1109/ACCESS.2024.3400919

RESEARCH ARTICLE

Kabsch Marker Estimation Algorithm–A Multi-Robot Marker-Based Localization Algorithm Within the Industry 4.0 Context

JOÃO BRAUN[1,2,3], JOSÉ LIMA[1,3,4], ANA I. PEREIRA[1,4], AND PAULO COSTA[2,3]

[1]Research Centre in Digitalization and Intelligent Robotics (CeDRI), Instituto Politécnico de Bragança, 5300-252 Bragança, Portugal
[2]Faculty of Engineering, University of Porto, 4200-465 Porto, Portugal
[3]Institute for Systems and Computer Engineering, Technology and Science (INESC TEC), 4200-465 Porto, Portugal
[4]Laboratório Associado para a Sustentabilidade e Tecnologia em Regiões de Montanha (SusTEC), Instituto Politécnico de Bragança, 5300-252 Bragança, Portugal

Corresponding author: João Braun (jbneto@ipb.pt)

This work was supported in part by the Foundation for Science and Technology (FCT), Portugal, through National Funds FCT; Ministry of Science, Technology and Higher Education (MCTES), and Programa de Investimento e Despesas de Desenvolvimento da Administração Central (PIDDAC) to the Research Centre in Digitalization and Intelligent Robotics (CeDRI), under Grant UIDB/05757/2020 (DOI: 10.54499/UIDB/05757/2020), Grant UIDP/05757/2020 (DOI: 10.54499/UIDP/05757/2020); and in part by Associate Laboratory for Sustainability and Technology in Mountains Regions (SusTEC) under Grant LA/P/0007/2020 (DOI: 10.54499/LA/P/0007/2020). The work of João Braun was supported by the FCT Foundation through the FCT Ph.D. Scholarship under Grant 2023.04536.BD.

ABSTRACT This paper introduces the Kabsch Marker Estimation Algorithm (KMEA), a new, robust multi-marker localization method designed for Autonomous Mobile Robots (AMRs) within Industry 4.0 (I4.0) settings. By integrating the Kabsch Algorithm, our approach significantly enhances localization robustness by aligning detected fiducial markers with their known positions. Unlike conventional methods that rely on a limited subset of visible markers, the KMEA uses all available markers, without requiring the camera's extrinsic parameters, thereby improving robustness. The algorithm was validated in an I4.0 automated warehouse mockup, with a four-stage methodology compared to a previously established marker estimation algorithm for reference. On the one hand, the results have demonstrated the KMEA's similar performance in standard controlled scenarios, with millimetric precision across a set of error metrics and a mean relative error (MRE) of less than 1%. On the other hand, KMEA, when faced with challenging test scenarios with outliers, showed significantly superior performance compared to the baseline algorithm, where it maintained a millimetric to centimetric scale in error metrics, whereas the other suffered extreme degradation. This was emphasized by the average reduced results of error metrics from 86.9% to 92% in Parts III and IV of the test methodology, respectively. These results were achieved using low-cost hardware, indicating the possibility of even greater accuracy with advanced equipment. The paper details the algorithm's development, theoretical framework, comparative advantages over existing methods, discusses the test results, and concludes with comments regarding its potential for industrial and commercial applications by its scalability and reliability.

INDEX TERMS ArUco markers, automated warehouse, autonomous mobile robots, fiducial markers, ground truth system, industry 4.0, indoor localization.

I. INTRODUCTION

The indoor localization of Autonomous Mobile Robots (AMRs) in dynamic Industry 4.0 (I4.0) environments presents significant challenges, especially in the absence of GPS signals [1] and various obstructions. Addressing this challenge is crucial for efficiently operating AMRs in such settings. Previous methodologies, like the Local Marker Estimation Algorithm (LMEA) introduced in [2], have made notable strides in this domain. LMEA, which relies on three

The associate editor coordinating the review of this manuscript and approving it for publication was Li He.

fiducial markers to form an orthonormal basis for localization, has proven to be a foundational approach. However, its effectiveness is compromised in dynamic scenarios where visual obstructions due to personnel or machinery movements are prevalent. The algorithm's dependence on a few anchor markers also introduces vulnerabilities; incorrect installations can lead to significant system degradation, highlighting a critical limitation in its adaptability and reliability. This research introduces a novel approach tailored to overcome these challenges, leading to the development of the Kabsch Marker Estimation Algorithm (KMEA). KMEA contributes to marker-based localization for AMRs by utilizing all visible markers within the environment, thus significantly improving robustness against visual obstructions—a notable weakness of its predecessor, LMEA. KMEA also has two more notable features, one being that it does not require the camera's extrinsic parameters, providing versatility that is welcomed in such chaotic scenarios. It is also less sensitive to marker misplacement during the installation stage of the workspace adaptation since it seeks the optimal transformation matrix between the markers in the real world and those in the image plane. Thus, by incorporating the Kabsch Algorithm, KMEA aligns detected fiducial markers with their known positions to enhance localization accuracy, providing reliable pose (position and orientation) estimates. This system has been tailored for multi-robot indoor localization, and it can act as a ground truth system for validating AMR localization methodologies. Its superiority over LMEA is demonstrated through rigorous testing in an I4.0 automated warehouse mockup, showcasing millimetric to centimetric accuracy and robust performance under extreme conditions. The mean relative error (MRE) of approximately less than 1.4% relative to the factory mockup's largest dimension indicates a highly accurate and predictable system. The algorithm's flexibility, error resilience, and performance using cost-effective hardware lay the groundwork for broader applications beyond the initial industrial context, including augmented reality and other visual positioning systems.

Thus, the main contributions of this paper are:

- Development of the KMEA, a new marker-based localization algorithm, integrating the Kabsch-Umeyama Algorithm, also known as the Kabsch Algorithm, for enhanced accuracy and precision. This represents a significant advancement over LMEA by addressing its core limitations and establishing a more robust and adaptable solution.
- Establishment of a solid theoretical framework for KMEA, extending and improving upon its predecessor. This framework includes a comprehensive and rigorous testing methodology, ensuring thorough validation and reliability of the algorithm.
- Demonstrated effectiveness of KMEA in a practical scenario, specifically in an I4.0 Automated Warehouse mockup.

The paper is organized as follows. After this introduction, Section II reviews relevant literature. Section III details the research work's methodology. Section IV describes the development of the KMEA and its predecessor. Section V presents the results and their implications. Finally, Section VI concludes the paper, discussing the significant findings and suggesting directions for future research.

II. RELATED WORK

Fiducial markers have firmly established themselves as indispensable in robotics, demonstrating value across diverse applications thanks to their versatility and efficacy. Particularly in localization tasks, they have proven to be a reliable tool, significantly enhancing the precision and adaptability of robotic systems in various settings. This section explores a variety of studies that have skillfully employed fiducial markers, underscoring their essential contribution to the progression of robotic technologies. The collected works highlight the markers' broad applications and their substantial impact, all while emphasizing the emerging importance of integrating visual markers with inertial sensors for localization and mapping. This fusion is crucial, particularly in enhancing the performance and reliability of AMRs in complex environments like automated warehouses and factory floors.

The ArTuga project introduces advancements in aerial robotics, specifically for precise unmanned aerial vehicles' vertical takeoffs and landings in challenging environments. It features an advanced multimodal fiducial marker, improving landing precision under diverse lighting and weather conditions, essential for continuous operations [3]. Developing a novel object pose estimation technique using pentagonal fiducial markers for enhanced detectability and accuracy presents a forward-thinking approach to marker design [4]. MechaTag, a mechanical fiducial marker system for harsh industrial settings, is introduced by Digiacomo et al. [5], showcasing high reliability in marker recognition. Zhang et al. [6] introduced a visual-marker-inertial fusion system utilizing sliding window optimization to tackle the challenges of visual-inertial odometry, demonstrating enhanced global localization accuracy, particularly in weak texture conditions and highlighting its application potential in I4.0 settings. Popovic et al. [7] and Alabbas et al. [8] have both made strides in human-robot collaboration in warehouse settings, focusing on reliable human localization for safety and operational efficiency and introducing innovative solutions such as wearable cameras and haptic feedback wearable robots.

Additionally, innovations in autonomous logistics, such as using fiducial markers for real-time pallet detection and tracking, highlight the practical implications of marker systems in dynamic industrial environments [9]. Braun et al. [2] contributed to AMR localization in industrial settings through the RobotAtFactory 4.0 (RAF) competition by presenting an indoor localization system that uses an Extended Kalman Filter and ArUco markers. Separately, Romero et al. [10] focused on a different aspect of AMR technology by developing a validation strategy for target-based vision

tracking systems. Zhang et al. [11] developed a precise visual positioning method for agricultural robots in greenhouses, using fiducial markers to enhance accuracy and minimize reprojection errors. Their technique significantly improves positioning precision compared to traditional methods. Also, Zhang et al. [12] tackle autonomous navigation challenges in indoor environments with a graph-based simultaneous localization and mapping (SLAM) method assisted by visual markers, achieving enhanced positioning accuracy and robustness. Huang et al. [13] and Yang and Yang [14] have explored optimization techniques for visual localization and multi-sensor fusion positioning systems, showcasing significant improvements in localization accuracy and system robustness, even in dynamic environments. In addition, the introduction of an optimized marker placement algorithm demonstrates significant improvements in localization accuracy by up to 20 per cent through strategic marker placement [13]. Analytical models for estimating pose estimate variances from fiducial markers are presented by Adamek et al. [15]. Huang et al. [16] provide a comprehensive review of indoor positioning systems for mobile robots, detailing current trends and developments where fiducial markers have their place.

Furthermore, a comprehensive evaluation of fiducial marker systems reveals their diverse applicability across robotics applications [17]. Machine learning approaches for robot localization using fiducial markers are introduced by Klein et al. [18], achieving millimetre-scale error in pose estimation. Kim et al. [19] and Ekici et al. [20] present novel solutions for localization and object tracking in dynamic environments, utilizing multi-layered 3D scan-matching, virtual fiducial markers and robust object pose tracking algorithms. In Micro Aerial Vehicle localization, Kirsch et al. [21] use fiducial markers for high-precision map creation and navigation in indoor environments.

Our research introduces the KMEA, reflecting on the varied applications and innovations in using fiducial markers for robotic localization. There is a discernible gap in the literature where detection methods of fiducial markers still need to be improved, even though some examples exist. Typically, it is found in contributions applications of visual information from fiducial markers for more complex localization systems. Thus, our contribution delves into two scopes of the literature. On the one hand, it presents a new detection method for fiducial markers by applying the Kabsch Algorithm. On the other hand, it also presents an application as a localization system tailored to AMRs' localization. It uses fiducial markers as the primary tool for localization in robotics, which has notable features, accuracy, and precision. As such, KMEA is a specialized solution for tailored environments, such as I4.0 warehouses or other similar scenarios, acting as a standalone localization system for a fleet of AMRs and a valuable component that can be integrated into broader detection systems, such as several research works cited in this section where the fiducial markers are just a part of a more complex localization system. Thus, our paper extends the capabilities and applications of localization using fiducial markers in modern robotics.

III. METHODOLOGY

The system was designed and assembled using as a case study a specific Portuguese Robotics Open competition, RAF.[1] The competition exemplifies I4.0 principles by showcasing AMRs that perform tasks autonomously in a simulated automated warehouse, reflecting the future of smart manufacturing. These robots navigate, recognize, and sort boxes using fiducial markers and communication protocols, demonstrating the essence of I4.0: digitalization, connectivity, and data-driven operations. This scenario highlights how robotic automation fosters efficiency, minimizes errors and optimizes manufacturing and logistics processes. Moreover, the competition promotes innovation and digital skills development, crucial for I4.0's focus on technological advancement and workforce transformation. For more details, the reader is encouraged to read more about it in the link provided in the footnote, and the research works [2], [22], [23]. Therefore, a top-view representation of the competition floor, a mockup of an automated warehouse within the I4.0 context with several ArUco markers placed, is displayed in Figure 1.

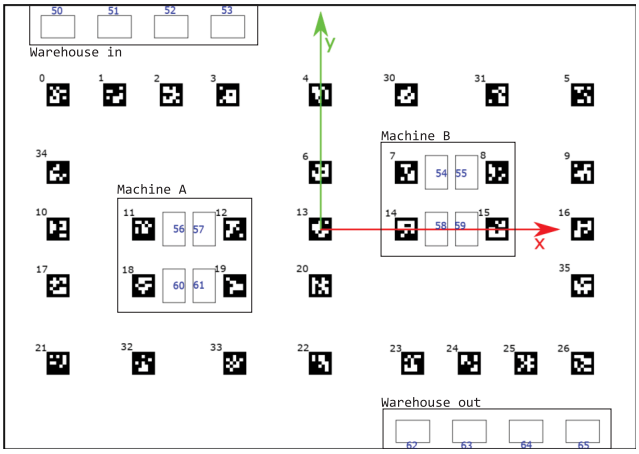

FIGURE 1. RobotAtFactory 4.0 factory floor mockup.

In Figure 1, the factory floor comprises an entrance, denoted by ''Warehouse in'', an exit, ''Warehouse out'', and two machines, ''Machine A'', and ''Machine B''. Each blank rectangle inside these sections represents positions where boxes can be removed or taken in for subsequent operations, such as transport and processes. Each number represents an ID of an ArUco marker, where the world frame is aligned with the marker 13 pose. As this illustration is a top-view perspective, the blue numbers represent the fiducial markers' IDs placed on the factory scenario's walls.

In addition, it is important to emphasize that when it is referred to the pose unless stated otherwise, it is expected to be assumed to be a 3D pose. When estimating the robots' poses, it is only necessary to compute the 2D pose of them,

[1] https://www.festivalnacionalrobotica.pt/2023/en/robotfactory-4-0-en/

that is, (x, y, θ). Finally, only the 2D position of the assessed markers will be evaluated (x, y) since their orientation is derived from their 2D position.

A. EXPERIMENTAL SETUP

The experimental setup comprises the RAF structured assembly in the laboratory, a physical replica of the official factory floor displayed in Figure 1. Figures 2a and 2b displays the testing scenarios where the camera's extrinsic parameters were changed.

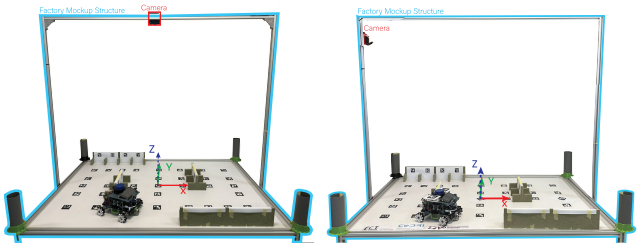

(a) Test scenario one. (b) Test scenario two.

FIGURE 2. RobotAtFactory 4.0 structure.

The factory floor was printed on canvas and followed the official dimensions of the competition floor, 1.7 × 1.2 m. In this sense, the markers' real poses follow the accuracy and precision of the printer. In addition, the poses of the markers used as ground truth were the ones made available on the official map. Thus, Figure 2 displays the assembled factory floor on the structure delineated in light blue. The camera, outlined in red, is mounted on the central part of the structure in scenario one, pointing downwards, approximately pointing at the central part of the factory scenario. In scenario two, the camera is positioned at the top-left part of the structure, pointing at the factory floor's origin. There is a coordinate frame drawn on the central part of the floor. It represents the world coordinate frame (on top of ArUco marker 13).

B. SYSTEM ARCHITECTURE

The research work's system architecture is designed around a Raspberry Pi 4B, strategically positioned to monitor the factory floor, as illustrated in Figure 2. This device serves as the central node for the detection of ArUco markers. It is equipped with a Raspberry Pi Camera Module 2 that continuously records video frames. These frames are subsequently analyzed to identify ArUco markers within its field of view (FoV) and to estimate their relative poses. This pose estimation process uses the intrinsic parameters of the camera and distortion coefficients to estimate the position and orientation of each marker detected accurately.

In this setup, the Raspberry Pi executes a Python script that uses OpenCV for image processing and ZeroMQ for networking. This script processes the captured video frames by converting them to grayscale, detecting ArUco markers, and calculating their poses. The data, including the estimated poses and marker IDs, are packaged into a data packet. This packet is transmitted to a computer application through a ZeroMQ socket for further processing or analysis.

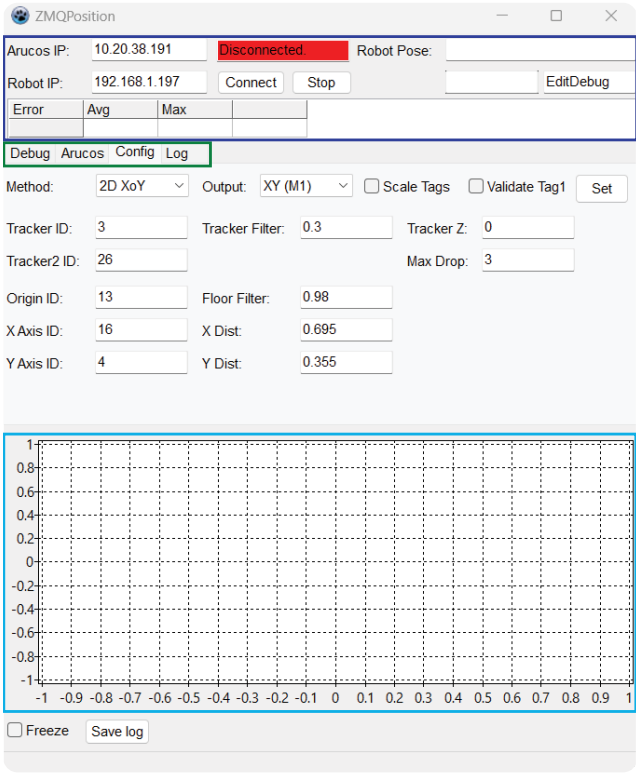

FIGURE 3. ArUco markers detection software's interface.

The computer application, represented in Figure 3, also developed as part of the research work, receives the data packets and further processes the pose information to obtain several metadata and the absolute poses of every detected marker. It can process the position of markers individually or as a pair. The latter option is to enhance the position estimation stability since computing the pose of the midpoint of a pair of markers is more stable than single markers since they are prone to measurement and quantization errors due to low resolution, illumination, and other external factors. Additionally, it also provides orientation estimation derived from the pair of markers. In this research context, these selected markers, or pairs, represent AMRs in the factory. Thus, based on the configuration settings, the application can also relay the pose information to an AMR or a fleet of robots, facilitating real-time interaction and navigation on the factory floor. The data sent to the robots is formatted as a series of key-value pairs representing the robot pose's coordinates.

In Figure 3, three coloured rectangles delineate four sections of the software interface. The area inside the dark blue rectangle presents the interface's section related to the communication between the Raspberry Pi 4B system, the software running on the computer, and the IP of the AMR that will receive the pose data. This part also presents metadata relative to the current algorithm being executed, such as the average and maximum error of all markers' pose estimation

and the current position of the tracked marker or pose of the pair of markers. Additionally, there are several types of tabs delineated by the green rectangle, which modifies the content presented in the complement area of the total interface, i.e., the uncovered area by the rectangles. The user can check debug information, all the ArUcos' markers ground truth pose or their estimated pose, if they are being detected, their estimated pose, the error, and other types of information. The configuration tab is currently presented in the illustration. The log tab is responsible for recording the data stream for retrospective usage. Finally, the rectangle in light blue represents the 2D Cartesian graph that plots all the estimated absolute markers' poses and their respective error vectors (vectors that point in the direction of the markers' real poses), where their magnitude represents the error.

Additionally, as previously mentioned, the computer application offers functionality to record the stream of the markers' relative pose data, allowing for retrospective analysis and use. This feature ensures that the system is not just limited to real-time operations but also contributes to data-driven insights and improvements in subsequent iterations. Finally, the software allows storing the absolute pose data relayed to the robots in CSVs' files. Figure 4 displays a Data Flow Diagram (DFD) summarizing how the system interacts with external and internal entities.

In Figure 4, relative pose data refers to the markers' relative pose to the camera's frame, and absolute pose data refers to the markers' pose relative to the world frame.

C. VALIDATION METHODOLOGY

The validation methodology was separated into four stages. The first three stages of tests were performed in scenario one illustrated in Figure 2a and the fourth stage test was performed in scenario two delineated in Figure 2b.

- Part I: 2D position assessment of several floor ArUco Markers.
- Part II: 2D position assessment of several floor ArUco Markers with 20 cm height support (simulating an average height of an AMR).
- Part III: 2D position assessment of several floor ArUco Markers with some fiducial markers distorted.
- Part IV: 2D position assessment of several floor ArUco Markers with some fiducial markers heavily distorted and the camera's extrinsic parameters changed.

The assessed markers for Part I of the validation methodology were: (0, 3, 5, 10, 12, 15, 18, 21, 22, 26, 30, 35). In turn, for Part II, some markers could not be verified because of the height since these markers did not appear in the camera's FoV; in this way, the evaluated markers were: (5, 12, 15, 18, 22, 30, 33, 35). Part III consisted of evaluating the same set of markers of Part I plus marker 34. Finally, part IV comprised of assessing markers (0, 3, 5, 10, 12, 21, 22, 26, 30, 34).

Part I assessed the accuracy and precision of the novel algorithm, KMEA, proposed in this research work and the previous one developed in [2] for baseline comparison, LMEA. Standard error metrics were chosen to perform this evaluation. As previously mentioned, the accuracy and precision assessment was focused solely on the markers' positions, as these positions inherently determine their orientations. In this sense, several markers on the factory floor were chosen around the camera's FoV. The selection criteria considered their radial distance to the camera's optical centre. The markers were chosen to be very dispersed to assess the algorithm's accuracy even with radial and transversal distortions that lens cameras have. Markers 4, 13, and 16 were excluded from the selection process to ensure fairness in the comparison since the previous approach uses these markers for pose estimation.

In this way, during Part I, for each marker and algorithm, 256 samples were measured. Figure 5 displays the detection software working during the Part I test.

Part II comprised assessing the same metrics; however, changing the z position of the estimated marker to mimic the height of an AMR developed for this scenario. Therefore, a 20 cm high support was designed and 3D printed to accurately position the assessed marker at 20 cm of height. Figures 6a and 6b show the support outlined in light blue and the support deployed on the test scenario, respectively.

It is also important to note that for the KMEA, each evaluated marker was removed from the algorithm's computations since it would be disingenuous to estimate its pose if it used its ground truth pose during the calculations. Also, markers 4, 13, and 16 were not considered for the previous reasons stated in this subsection.

As it is possible to see in Figure 6, the bottom part of the support has a gap to neatly fit an ArUco marker from the floor. This support was put on top of every selected marker of this validation part. In the same way as Part I validation, 256 samples were taken for each marker and algorithm, and statistical metrics were computed.

Part III validation assessed their robustness, one of the most important aspects of a localization system. The previous algorithm, presented in [2], has one limitation, as previously mentioned: it depends on three markers to generate the orthonormal basis for the world's frame. However, suppose one or more of them are incorrectly placed or occluded, which can happen in dynamic scenarios such as industrial warehouses. In that case, it can generate errors in estimating the detected markers, including the tracked ones. KMEA does not have this flaw since it takes the information of all detected markers in a given time to estimate the pose of all the detected markers. This information can be acquired with noise and other sources of error from these detected markers. Thus, this information must be considered when designing filters for the system if the conditions surrounding the system or the system itself are highly noisy. Thus, Part III of the validation methodology was to print markers 4, 13, and 16 of the same size, place them on top of their respective counterparts on the factory floor, and distort them by moving and rotating a little to generate errors in the estimation process. This principle will stress out both algorithms, however much more

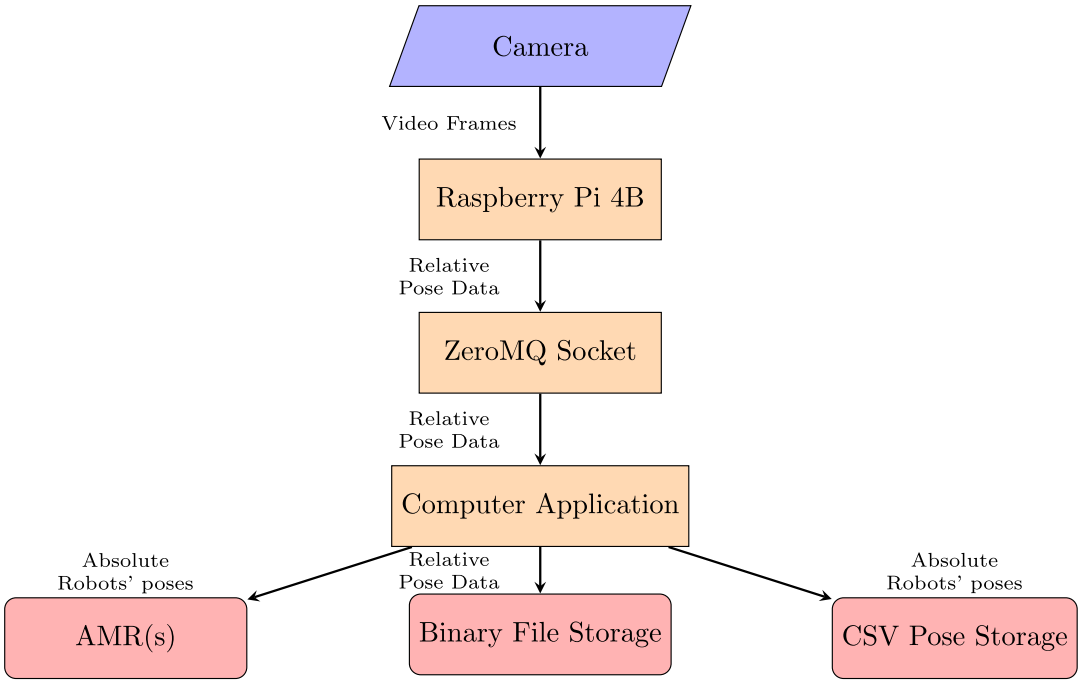

FIGURE 4. Data flow diagram describing the system's data flow during the pose estimation process.

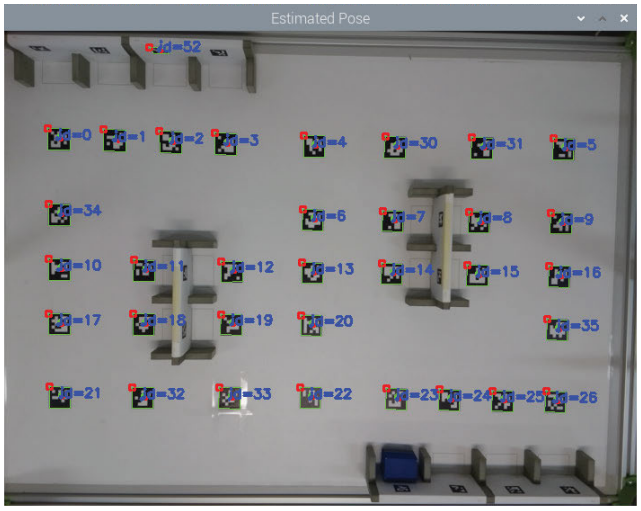

FIGURE 5. ArUco detection software - part I validation.

the predecessor to showcase its vulnerability. After that, the two algorithms were assessed similarly to the other parts of the validation methodology, retrieving 256 samples for each marker and each algorithm and computing the respective statistical metrics.

Figure 7 shows the Part III validation scenario configuration, with the printed markers outlined in light blue. It was decided not to distort other markers than the three ones used by the LMEA (4, 13, 16) for estimation because the test was not going to add any value to the research work since LMEA would not be affected by them. Instead, it would just misestimate the distorted markers. The point of this test is to show that the LMEA is heavily dependent on only three markers, which is not robust, in contrast to the novel, which does not have this caveat.

Finally, Part IV of the validation methodology was to perform tests in similar conditions as Part III; however, the camera's extrinsic parameters changed, as explained at the beginning of this subsection. The objective of the Part IV tests was to display the robustness of the KMEA under a different scenario and to illustrate that it is independent of the camera's extrinsic parameters. Therefore, the assessed markers and the camera's extrinsic parameters were changed. Part III's set of distorted tags remains the same, although with different distortions. Figure 8 displays a captured frame of the camera under scenario two of testing; the light blue rectangles delineate the distorted tags. The AMR was not present on the table during testing.

IV. ArUco MARKERS LOCALIZATION ALGORITHMS

In this research, it was employed two distinct algorithms for estimating the positions of ArUco markers within the camera's FoV, a critical aspect for accurate and reliable localization in robotic applications. The algorithms are LMEA and KMEA. The latter is the primary focus of our validation efforts in this study due to its robustness, while the former has been validated in previous work [2]. It is important to note that both algorithms assume that the frames have square-shaped pixels for scaling purposes.

A. THE LOCAL MARKER ESTIMATION ALGORITHM

The LMEA transforms the poses of detected ArUco markers from the camera's coordinate system to a world coordinate system. It leverages three reference markers or anchors — the

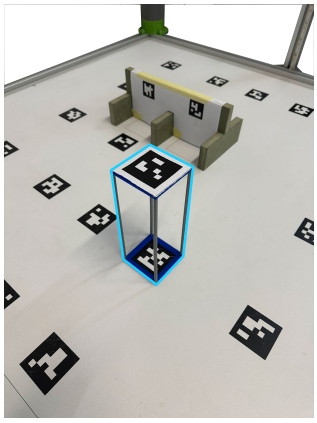

(a) Height support.

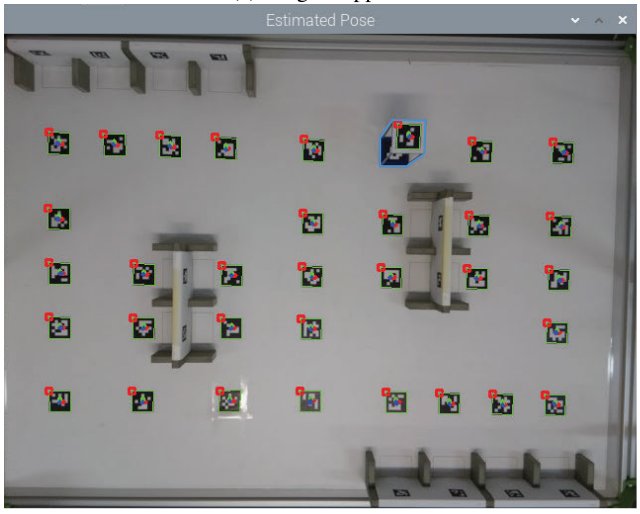

(b) ArUco Detection Software - Part II validation.

FIGURE 6. Part II validation.

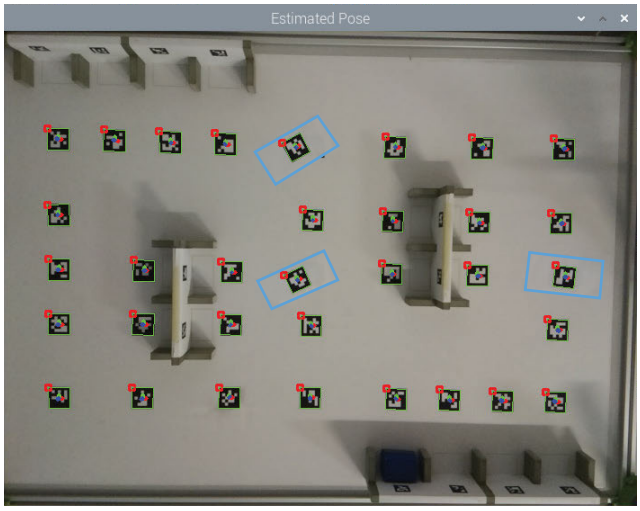

FIGURE 7. ArUco detection software - part III validation.

origin, X-axis, and Y-axis markers. LMEA computes a scale factor based on the known distance along the X-axis, which is the X-axis anchor position, computes a rotation matrix for

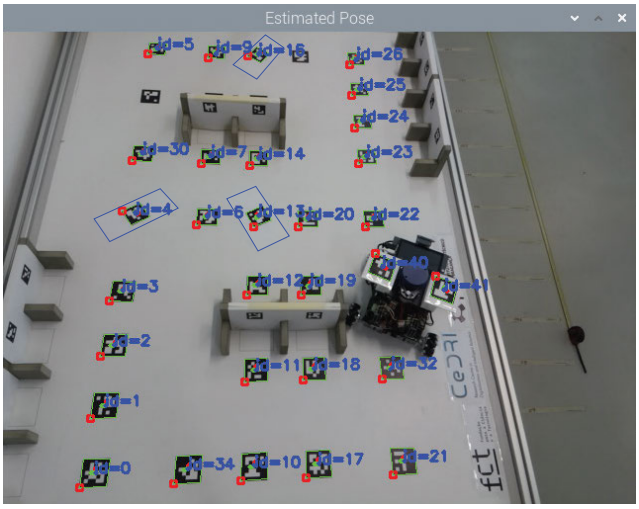

FIGURE 8. ArUco detection software - part IV validation.

alignment and applies these transformations to all detected markers. For an in-depth description and validation of the algorithm, readers are directed to [2].

The LMEA proceeds in three main stages:

1) **Scale Calculation:** Computes a real linear scale factor using the known distance *XDist* and the camera-estimated distance between the origin and X-axis markers.
2) **Translation and Initial Scaling:** Scale and translate the positions of all detected markers relative to the origin.
3) **Rotation Adjustment:** Calculates a proper orthonormal basis that represents the world's coordinate frame with the versors derived from the scaled anchor markers and composes a rotation matrix with it. Next, it applies the rotation matrix to align all markers relative to the origin.

For a comprehensive understanding of the algorithm, Figure 9 shows the process of the algorithm,

where the legend is presented below the algorithm's inputs, outputs, constants, methods, and variables. Soon after, Algorithm 1 describes the inner details of the flowchart processes.

1) ALGORITHM'S INPUTS

- All ArUco Markers' relative poses to the camera.
- Ground truth pose of three anchors ArUco Markers to form an orthonormal basis.

2) ALGORITHM'S OUTPUTS

- All ArUco Markers' estimated absolute poses (configurable).
- Robots' poses (configurable).

3) KEY VARIABLES

- *sc*: Scalar used to adjust the real positions of the markers in the world's frame.

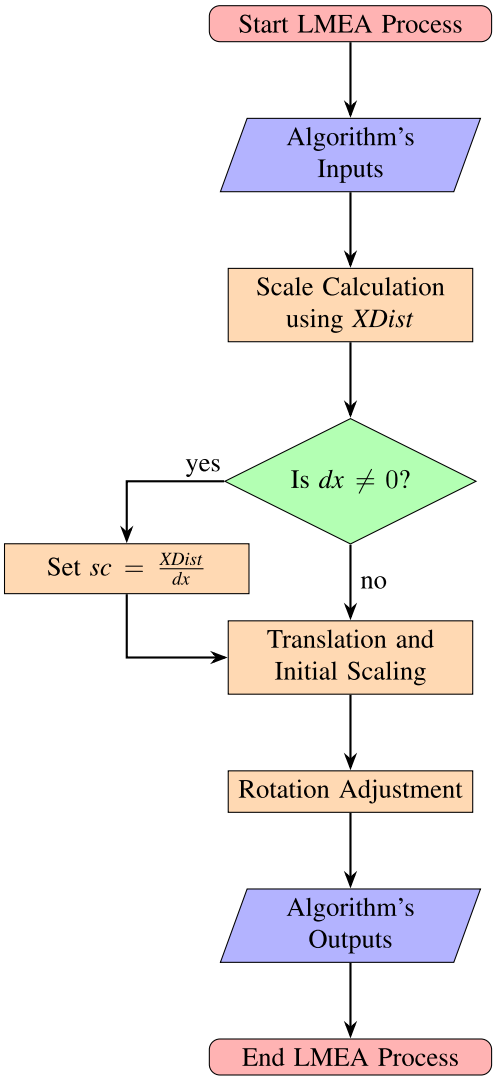

FIGURE 9. Flowchart of the LMEA process.

- V3N: Computes the magnitude of a vector.
- dx: Norm of the vector pointing from the origin to the X-axis marker anchor in the camera's coordinate system.
- pO: Origin point of the world's frame.
- pX: X-axis marker anchor point in the world's frame.
- Vr($startP$, $endP$): Method to compute a unit vector from startP to endP.
- $XDist$: x-axis distance of the X-axis marker anchor.
- $MkDiff$: Translation operation relative to the origin marker.
- $originID$: Identifier for the origin anchor marker.
- $Mks[i].Pcam$: Pose of the i-th marker in the camera's coordinate system.
- $Mks[i].Pw$: Pose of the i-th marker in the world's coordinate system.
- $[VrX, VrY, VrZ]$: $[x, y, z]$-axes versors of the world's coordinate frame.
- $XAxisID$: Identifier of the X-axis anchor marker.
- $YAxisID$: Identifier of the Y-axis anchor marker.
- V3ExtP: Method to compute the external product between two 3D vectors.
- calcRM: Method to compute the 3D rotation matrix given a set of versors in $[x, y, z]$.
- R: Rotation matrix for aligning the coordinate systems.

Algorithm 1 Pseudocode - Local Marker Estimation Algorithm

```
procedure LMEAProcessTags
    sc = 1
    dx = V3N(pO, pX)

    if dx ≠ 0 then
        sc = XDist / dx
    end if

    for each eligible marker i do
        MkDiff = Mks[i].Pcam − Mks[originID].Pcam

        Mks[i].Pw = sc · MkDiff
    end for

    VrX = Vr(Mks[XAxisID].Pw)
    VrY = Vr(Mks[YAxisID].Pw)
    VrZ = V3ExtP(VrX, VrY)
    VrY = V3ExtP(VrZ, VrX)

    R = calcRM(VrX, VrY, VrZ)

    for each eligible marker i do
        Mks[i].Pw = R^T · Mks[i].Pw
    end for
end procedure
```

B. THE KABSCH MARKER ESTIMATION ALGORITHM

The KMEA advances ArUco marker-based localization by utilizing all detected markers to compute the transformation matrix between the detected markers and their actual real-world positions. This approach improves pose estimation accuracy within a global coordinate system and addresses the challenges of indoor localization for AMRs in Industry 4.0 environments. By employing the Kabsch Algorithm, KMEA finds the optimal alignment of the poses of markers detected by the camera with their real-world coordinates. Notable features of KMEA include its operation without needing the camera's extrinsic parameters and its reduced sensitivity to marker misplacement.

The KMEA operates in three main stages:

1) **Scale Calculation:** First, KMEA proceeds to iterate over all detected markers and compute the mean absolute distance of every marker relative to the origin marker. This computation is performed for the markers' camera-detected poses and their ground-truth poses. Subsequently, a scale factor is computed by the ratio

of these two mean absolute distances. Finally, the camera's markers poses are scaled with the computed scale factor.

2) **Optimal Rotation Matrix Calculation:** The next step of the algorithm is the computation of the optimal rotation matrix between the two sets of points. Therefore, two matrices of the Kabsch Algorithm, P and Q, are populated with the camera's scaled markers poses and their ground-truth counterparts, respectively. The markers used in these matrices are identified as eligible after being checked for computation suitability. Afterwards, the z coordinate of the ground truth markers poses is injected with a random noise mean 0 and amplitude $[-0.5, 0.5)$, scaled by a factor of 0.0001. This operation is done to avoid degeneracies during the computations of the Kabsch Algorithm that comes with the possible coplanarity or colinearity of the markers. Soon after, the optimal rotation matrix between the two sets of points is computed, R, with the centroids, $[Po, Qo]$ of the matrices P and Q, respectively. The determinant of R is checked if it is -1; if so, the z-axis of the rotation matrix is flipped to ensure proper rotation. For more information about the Kabsch Algorithm, the readers are referred to [24].

3) **Coordinate frame transformation:** The algorithm's last step comprises two translations and one rotation (not in this order). First, each camera's scaled detected marker is translated to its origin marker in the camera frame (Po), and then it is rotated to the world's frame. Finally, it is translated to the world's origin marker position (Qo).

For a comprehensive understanding of the algorithm, Figure 10 shows the process of the algorithm.

Where below you will find the algorithm's legend. Soon after, Algorithm 2 describes the inner details of the algorithm's logic.

1) ALGORITHM'S INPUTS

- All detected ArUco Markers' camera poses.
- Ground truth poses of all ArUco Markers.

2) ALGORITHM'S OUTPUTS

- All ArUco Markers' estimated absolute poses (configurable).
- Robots' poses (configurable).

3) VARIABLES EXPLANATION

- N: Counter.
- V3N: Method to compute the norm of a 3d vector.
- $OriginID$: The origin ArUco Marker identifier.
- sc: Scaling factor for aligning detected marker positions with real-world coordinates.
- $Mks[i].Pcam$: Camera-detected pose of the i-th marker.
- $Mks[i].Pw$: World pose of the i-th marker.
- $Mks[i].Preal$: Ground truth pose of the i-th marker.

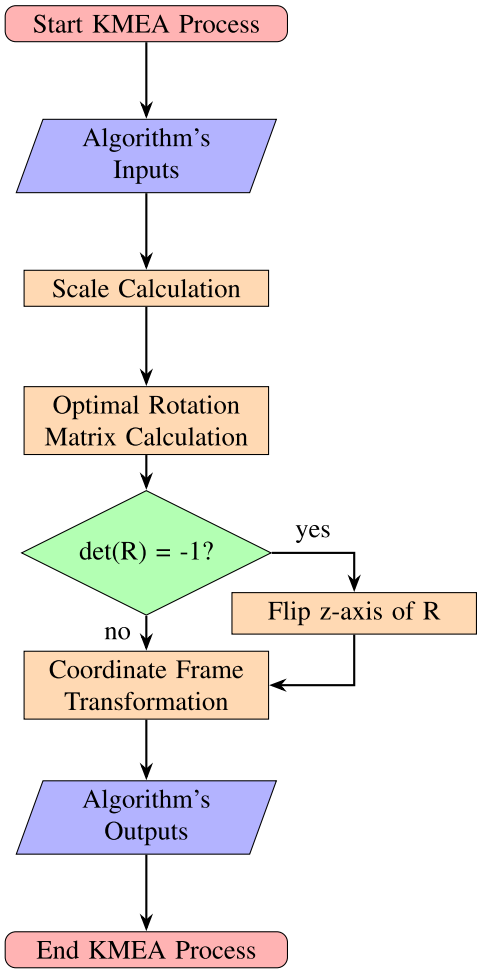

FIGURE 10. Flowchart of the KMEA process.

- dx, drx: Mean absolute distances between markers in camera and real coordinates.
- P, Q: Matrices with scaled world camera and real positions of eligible markers, respectively.
- Rnd: Random number generator from [0, 1).
- OptRotMat(P, Q): Kabsch-Umeyama Algorithm returns the optimal rotational matrix between the sets of points of matrices P and Q.
- R, Po, Qo : Optimal rotation matrix and the centroids from the matrices P and Q, respectively.
- det(R): Method that returns the determinant of a matrix.
- $ILeft$: 3D identity matrix with the element $a_{2,2}$ flipped to reflect the z-axis.

C. THEORETICAL ADVANTAGES OF THE KMEA OVER THE LMEA

The KMEA demonstrates several theoretical advantages over the LMEA. Key benefits include enhanced robustness, superior alignment between coordinate systems, independence from specific markers, less sensitivity to marker misplacement, a comprehensive global optimization strategy incorporating all visible markers for more precise estimations, and independence from the camera's extrinsic

Algorithm 2 Pseudocode - Kabsch Marker Estimation Algorithm

procedure KMEAProcessTags
  $N = 0$
  for each eligible marker i **do**
    $dx = dx + \text{V3N}(Mks[i].Pcam - Mks[OriginID].Pcam)$
    $drx = drx + \text{V3N}(Mks[i].Preal - Mks[OriginID.Preal])$
    $N+ = 1$
  end for
  if $N \neq 0$ **then**
    $dx = \frac{dx}{N}$
    $drx = \frac{drx}{N}$
    if $dx \neq 0$ **then**
      $sc = \frac{drx}{dx}$
    end if
  end if
  for each eligible maker i **do**
    $Mks[i].Pw = sc \cdot Mks[i].Pcam$
    $P[i, :] = Mks[i].Pw$
    $Mks[i].Preal[2, 0]+ = 1e - 4 * (Rnd - 0.5)$
    $Q[i, :] = Mks[i].Preal$
  end for
  $[R, Po, Qo] = \text{OptRotMat}(P, Q)$
  if $\det(R) < 0$ **then**
    $R = R * ILeft$
  end if
  for each eligible marker i **do**
    $Mks[i].Pw = R^t \cdot (Mks[i].Pw - Po^t) + Qo^t$
  end for
end procedure

parameters. It is essential to note that these algorithms' efficacy largely depends on the accuracy of the camera calibration. Meticulous calibration can mitigate errors influenced by distortions during data acquisition for these algorithms. Thus, this study's camera underwent a standard calibration technique, and the calibration results were acceptable. Consequently, no complex filters or outlier rejection algorithms were developed, except for a first-order infinite impulse response filter applied to both algorithms to mitigate noise.

D. INTEGRATION WITH AMRs

The robot's pose can be estimated individually or with a pair of markers, depending on the configuration of the software.

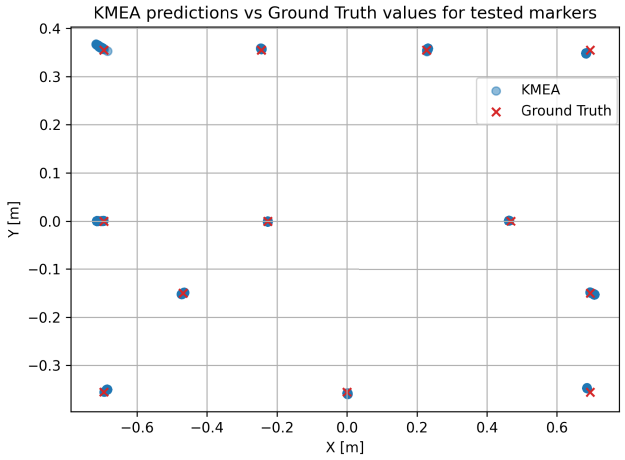

(a) Scatter plot of KMEA and ground truth values.

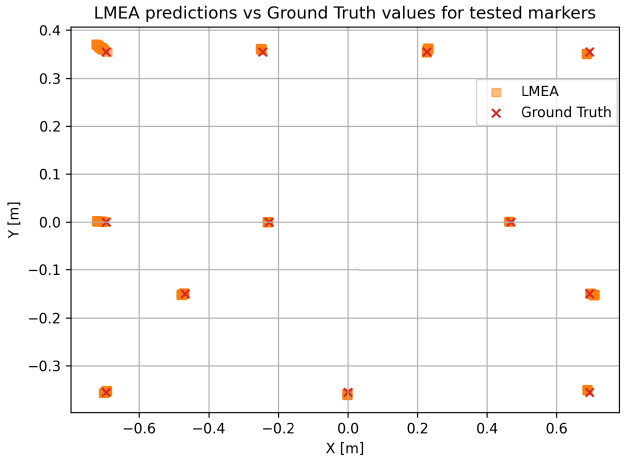

(b) Scatter plot of LMEA and ground truth values.

FIGURE 11. Part I - comparative scatter plots of markers' position estimations by KMEA and LMEA.

When configured for individual marker pose estimation, the algorithm directly takes the position of a single specified marker as the robot's position. This method is straightforward but relies on that specific marker's accurate detection and localization.

In the case of a pair of markers, the algorithm calculates the midpoint between the two markers to determine the robot's position. Also, the orientation is orthogonally calculated based on the line connecting the two markers. Thus, this method provides redundancy and can be more robust, as it does not rely on a single marker for pose estimation. In particular, it stabilizes orientation estimation more.

Finally, as mentioned in the algorithms' descriptions, the output of the algorithms can be configured; that is, it can just estimate the markers that represent the AMRs in an industry factory, for instance. In this case, it was configured to estimate all visible markers.

V. RESULTS AND DISCUSSION

A series of tests assessed the algorithms' performance, focusing on accuracy, precision, and robustness. As already

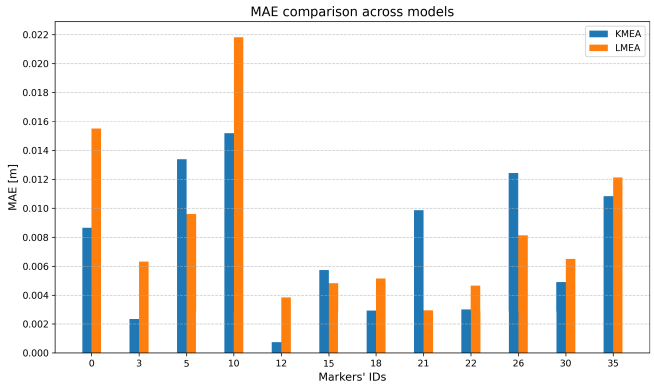

(a) Bar plot of MAE of both algorithms in the assessed markers.

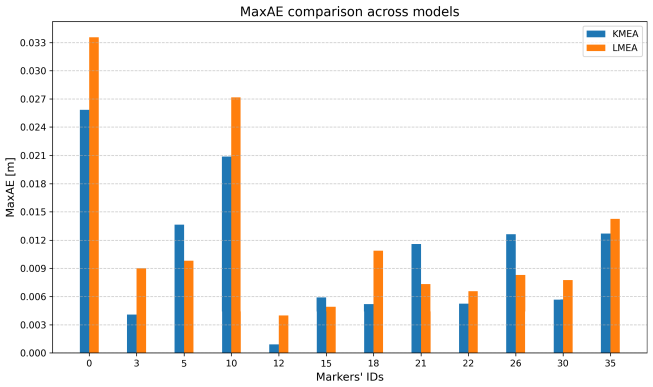

(b) Bar plot of MaxAE of both algorithms in the assessed markers.

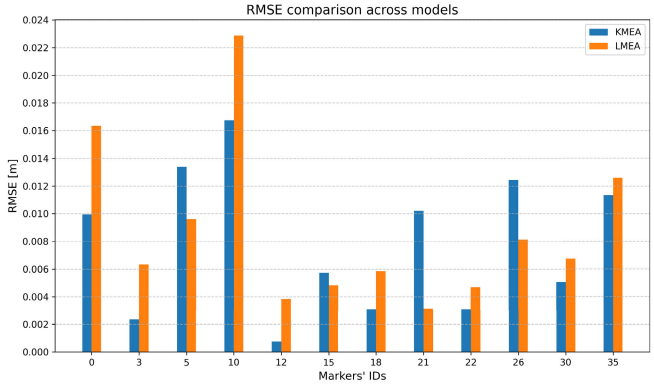

(c) Bar plot of RMSE of both algorithms in the assessed markers.

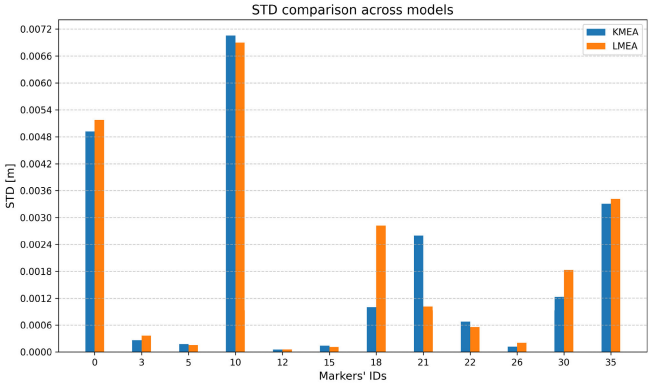

(d) Bar plot of STD of both algorithms in the assessed markers.

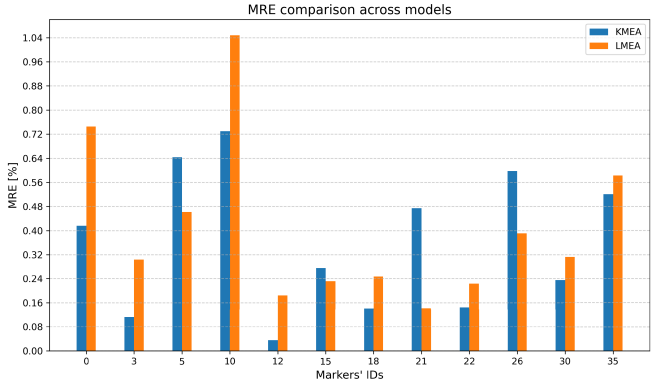

(e) Bar plot of MRE of both algorithms in the assessed markers.

FIGURE 12. Part I - bar plots of error metrics of both algorithms described in the test methodology.

stated, the validation methodology was divided into four parts.

A. PART I. SEVERAL MARKERS ESTIMATED UNDER NORMAL CONDITIONS.

The first part of the validation, as previously mentioned in Section III, was assessing both algorithms' error metrics under typical conditions in the testbed. Thus, several markers were chosen to assess the whole workspace captured in the images, excluding, for fairness, the specific markers that LMEA uses for localization. In this sense, 256 samples were taken for each analyzed marker for each algorithm. Figures 11a and 11b display scatter plots of the KMEA and LMEA against the markers' ground truth values, respectively.

Figure 11 shows a comprehensive and overall visualization of Part I validation. As these scatter plots cover the whole workspace and both algorithms are very accurate and precise, they do not show their proper performance with this low resolution. For this reason, several metrics were computed for Part I. Thus, Figure 12 shows the metrics root mean squared error (RMSE), mean absolute error (MAE), maximum absolute error (MaxAE), sample standard deviation (STD), and MRE for both algorithms as bar plots.

For a structured analysis, it is suggested to first visualize the MAE bar plot in Figure 12a. As illustrated, both algorithms show consistent errors in the millimetric range, with some markers having a centimetric range. The errors vary with the markers because they have different positions in the factory mockup and, therefore, in the image plane, causing potential diverse effects of deterministic and non-deterministic errors such as quantization, distortions, and noise, already discussed in Section III. In addition, the result bars of markers 0 and 10 showed the highest error metric. Two common characteristics of both markers are that they are on the edges of the camera's FoV and more distant from the camera's optical centre, making them more sensitive to the mentioned source of errors and distortions, especially the radial type of distortion. Nevertheless, the maximum MAE of the KMEA is 1.5 cm of error, and the LMEA is 2.2 cm. Moving on to metric MaxAE, both algorithms showed a consistent centimetric error below 2 cm, with two errors above 2 cm, markers 0 and 10, and LMEA again underperformed compared to the KMEA. The same interpretation of MAE can be applied to the RMSE bar plot since they have similar results. The latter metric is more sensitive to outliers because of the residuals' squaring process. However, since the errors were consistent with their averages and the scale is small, both metrics show similar results.

Regarding STD, the deviations were consistently below 0.7 cm, which shows that both algorithms are very precise, with a notable pattern with markers 0 and 10 having the worst results again. Finally, one important metric to assess is the MRE, which is the mean relative error to the highest dimension of the testbed, i.e., the factory mockup, expressed in percentage. Since the factory mockup has the shape of a rectangle of 1.7×1.2 m, the hypotenuse of it was used as the maximum dimension. Verifying the plot more closely, one can note that the highest error that the KMEA showed was 0.72%, with most of the errors being below 0.4%. In contrast, the highest error of LMEA was 1.04%, and most errors were below 0.4%.

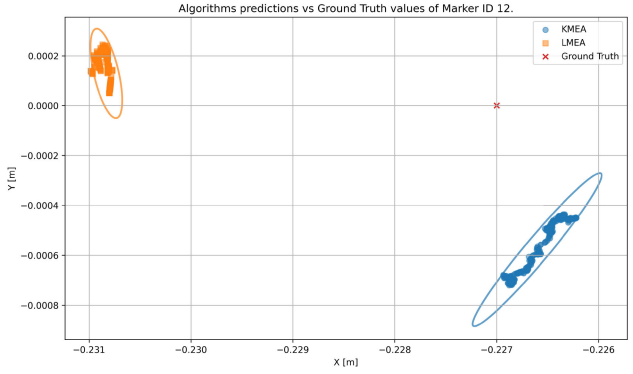

FIGURE 13. Part I - scatter plot of both algorithms and the ground truth position of marker ID 12.

Figure 13 displays the scatter plot of both algorithms of marker ID 12 in a zoomed scale to show more details about the estimations. The ellipses are confidence ellipses of three standard deviations where they were generated assuming a normal distribution of the samples (Central Limit Theorem). The KMEA samples can be seen in blue, and the LMEA in orange. The red "x" displays the ground truth position of marker 12. In this plot, it is possible to perceive that both sample distributions have low variance and bias relative to the actual value. Finally, Table 1 shows the error metrics' summary of Part I applied to both algorithms for better overall analysis.

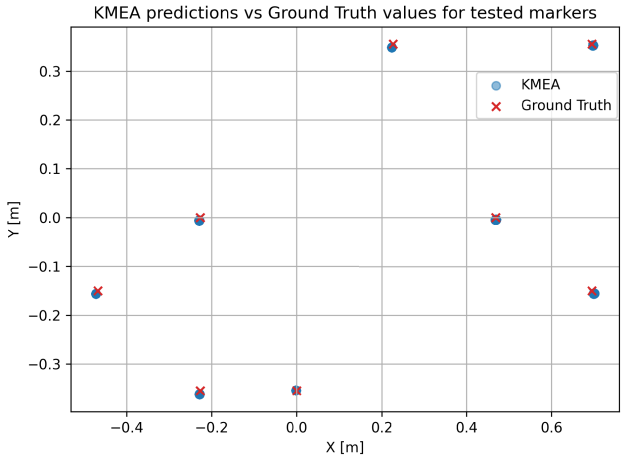

(a) Scatter plot of the markers' positions estimations of the KMEA against their ground truth values.

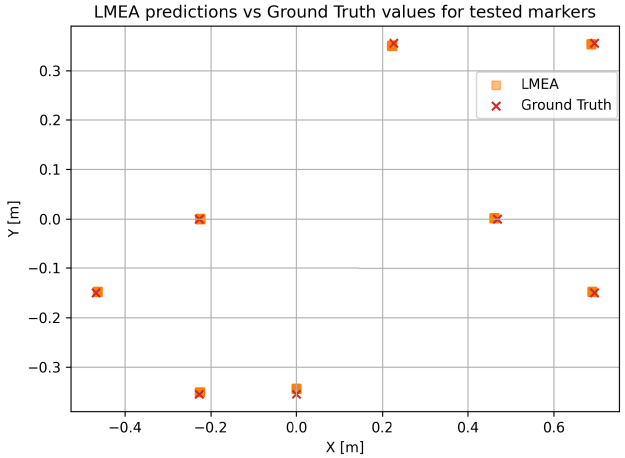

(b) Scatter plot of the markers' positions estimations of the LMEA against their ground truth values.

FIGURE 14. Part II - comparative scatter plots of markers' position estimations by KMEA and LMEA.

TABLE 1. Part I - comparison of estimation metrics. The percentage change computation is of KMEA relative to LMEA.

Metric	KMEA	LMEA	% Change
RMSE [m]	0.0078	0.0087	-10.3
STD [m]	0.0018	0.0019	-4.8
MAE [m]	0.0075	0.0084	-11.2
MaxAE [m]	0.0104	0.0120	-13.4
MRE [%]	0.3605	0.4060	-11.2

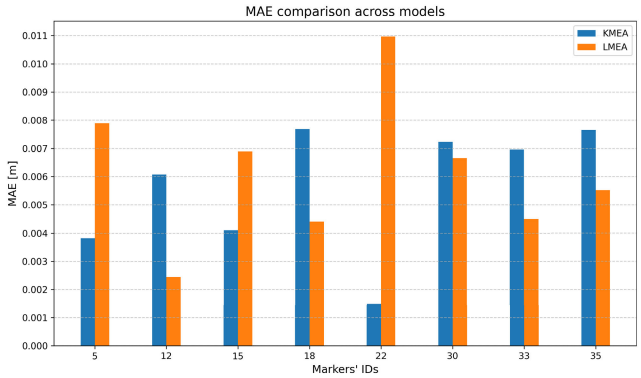

(a) Bar plot of MAE of both algorithms in the assessed markers.

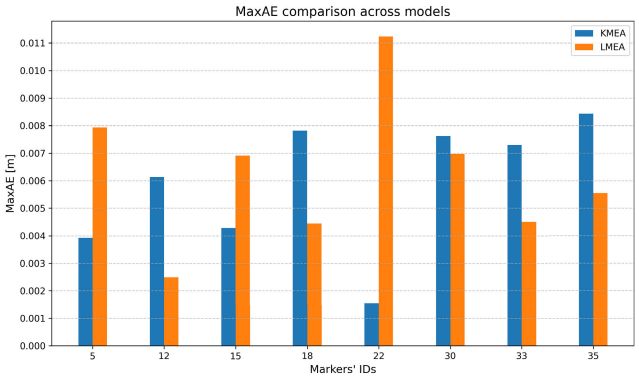

(b) Bar plot of MaxAE of both algorithms in the assessed markers.

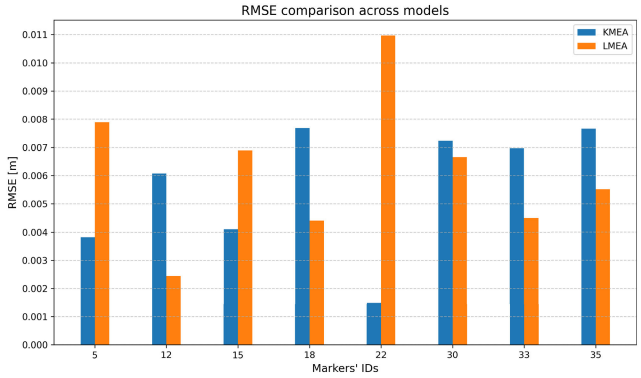

(c) Bar plot of RMSE of both algorithms in the assessed markers.

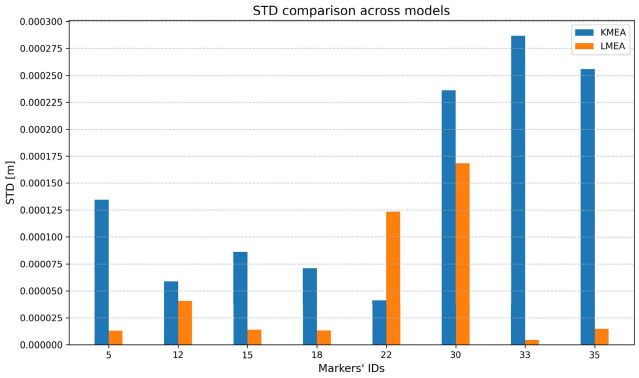

(d) Bar plot of STD of both algorithms in the assessed markers.

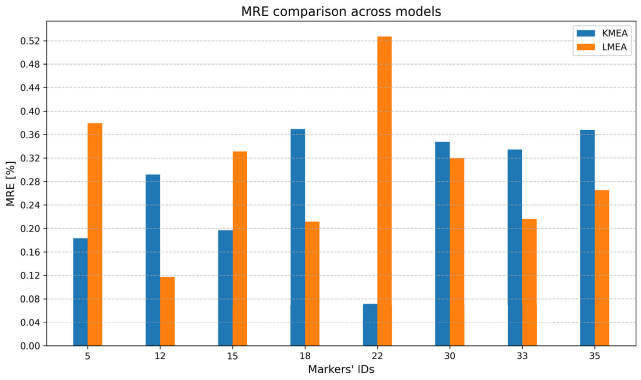

(e) Bar plot of MRE of both algorithms in the assessed markers.

FIGURE 15. **Part II - bar plots of error metrics of both algorithms described in the test methodology.**

As seen in Table 1, both algorithms presented very accurate and precise error metrics, indicating that they are both suited to be localization algorithms using fiducial markers. This is very emphatic because both MREs are in the order of 0.4%, and their other error metrics are millimetric. In addition, the percentage change between KMEA and LMEA was computed and presented in the column "% Change", where the former performed better in every error metric.

B. PART II. SEVERAL MARKERS ESTIMATED WITH A 20 CM HEIGHT SUPPORT

Part II is similar to Part I; however, a height support, displayed in Figure 6a, was used to assess the position estimations within a 20 cm height relative to the factory floor since this is the height of the AMRs used in this scenario. Thus, as the distance between the centre of the assessed marker and the optical centre of the camera is decreased, it is expected, in theory, that the error metrics will be reduced compared to the Part I test since all the sources of error already discussed in Section III will tend to be lower. In this reasoning, Figure 14 shows the scatter plots of both algorithms for the assessed markers.

Since these scatter plots give an overall view of the test, bar plots were also generated to assess the algorithms in the second part more thoroughly. Thus, Figure 15 shows all the five error metrics for the Part II test.

As illustrated in Figure 15, all metrics show that the estimations became more precise, denoted by the STD being practically zero across all estimated markers, and more accurate, hinted by all the other error metrics that had their values reduced in general. For a more comprehensive analysis, the errors metrics' summary is presented in Table 2.

TABLE 2. Part II - comparison of estimation metrics. The percentage change computation is of KMEA to LMEA.

Metric	KMEA	LMEA	% Change
RMSE [m]	0.0056	0.0062	-8.6
STD [m]	0.0001	0.0000	199.0
MAE [m]	0.0056	0.0062	-8.6
MaxAE [m]	0.0059	0.0063	-5.9
MRE [%]	0.2704	0.2960	-8.6

According to the table, the values were smaller in all metrics. Also, KMEA benefited more from the decreased marker distance to the camera's optical centre. This is corroborated by the percentage change that shows that the KMEA metrics are smaller than the KMEA metrics. However, these differences are negligible, and both algorithms have solid accuracy and precision for this case study. One different metric was the STD, displayed by the "% Change" column, which shows an increase of approximately 200 % of KMEA relative to LMEA. This value is disingenuous and does not represent the practical scenario since both values are minimal, corroborated by the LMEA value that does not even show considering the four decimal digits decided for display.

C. PART III. SEVERAL MARKERS ESTIMATED WITH ORTHONORMAL BASIS MARKERS DISTORTED

As explained in Section III, Part III methodology and objective is to evaluate the robustness of both algorithms by exploiting a critical weakness of the LMEA. Because this algorithm considers only three markers to form its orthonormal basis to estimate all the other markers, its performance is crucially tied to them. Therefore, if one or more of them are obstructed, damaged, worn out over time, or even wrongly assembled, it would significantly affect the accuracy and precision of the algorithm. If the obstruction happens for a limited amount of time, this can be mitigated with filtering and other approaches; however, with time, this would degenerate the error propagation. This is not the case for the KMEA, which can achieve the same or even better accuracy and precision with much more robustness. This can be even more magnified with a proper error distribution study for proper filtering and outlier rejection, proving an excellent choice for industrial and scalable applications. In this sense, Figure 16 shows the scatter plots of the algorithms against the ground truth values for a holistic view of the test.

This illustration visually represents the effects of the distortion of the markers, which affects the accuracy of the approaches, albeit much more impactful in LMEA. This discrepancy is more detailed in Figure 17, which shows all the metrics results from the Part III assessment.

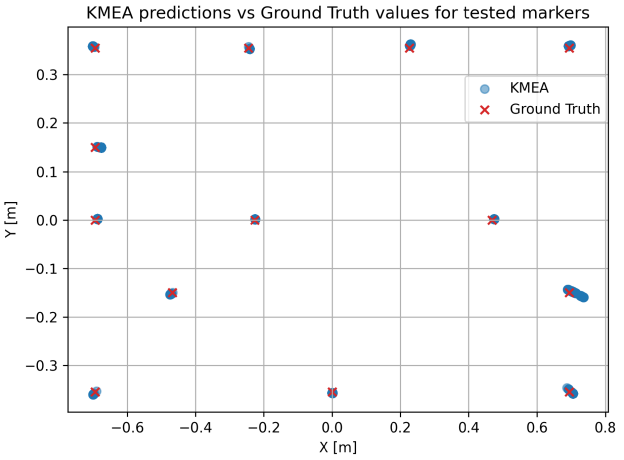

(a) Scatter plot of the markers' positions estimations of the KMEA against their ground truth values.

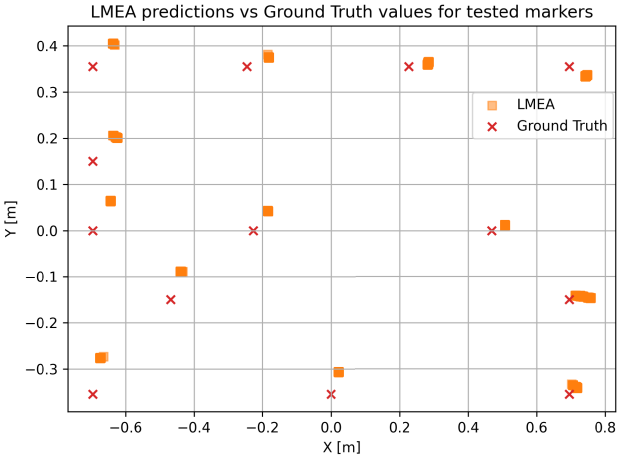

(b) Scatter plot of the markers' positions estimations of the LMEA against their ground truth values.

FIGURE 16. Part III - comparative scatter plots of markers' position estimations by KMEA and LMEA.

So, after misaligning the markers responsible for the orthonormal basis of LMEA, it is clear that both KMEA and LMEA are affected. However, the latter becomes unfeasible to be considered for a localization system since an error of more than a couple of centimetres could affect the parking operations in the warehouse mockup, as outlined by the error metrics reaching up to 8.8 cm of MAE, MaxAE, RMSE, and 4% of MRE. KMEA, despite three misaligned markers, can still yield acceptable results within this case study's constraints, with the MAE, RMSE, and MaxAE all below 1.6 cm. The worst-case scenario occurs with marker 35, where errors reach 4.0 cm, indicating an outlier since its estimation was significantly impacted in STD and MaxAE and moderately for the other metrics for both approaches. The MRE metric of KMEA also corroborates the outlier argument, where the metric stayed below 0.8% across all markers. Both algorithms remained precise, however, with a millimetric STD. This is expected since misaligning specific

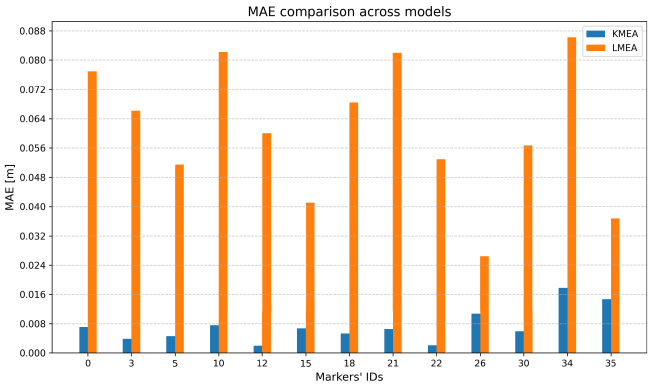

(a) Bar plot of MAE of both algorithms in the assessed markers.

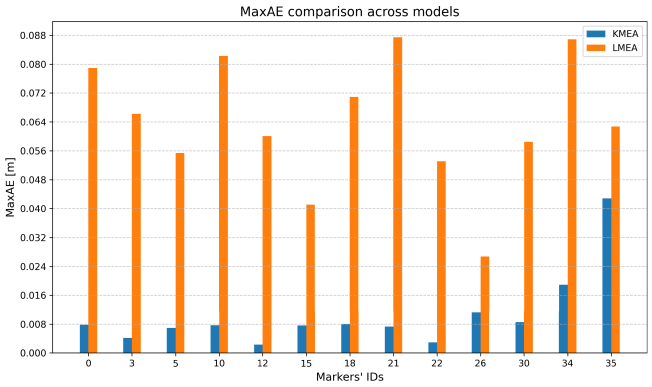

(b) Bar plot of MaxAE of both algorithms in the assessed markers.

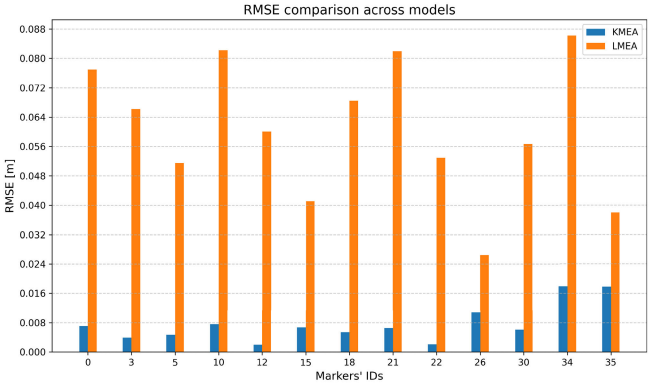

(c) Bar plot of RMSE of both algorithms in the assessed markers.

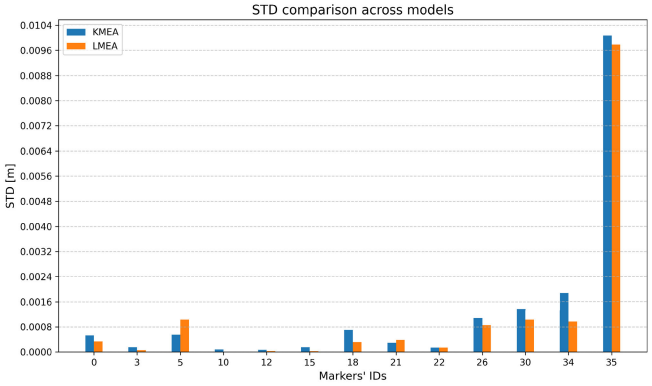

(d) Bar plot of STD of both algorithms in the assessed markers.

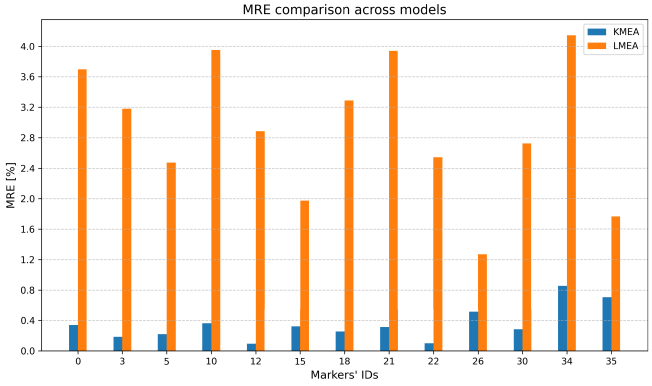

(e) Bar plot of MRE of both algorithms in the assessed markers.

FIGURE 17. **Part III - bar plots of error metrics of both algorithms described in the test methodology.**

markers would only jeopardize the estimation bias. Finally, marker 35 showed a massive spike in the STD metric for both algorithms, with a 1 cm deviation, compared to the other markers predominantly in the sub-mm scale, strengthening the case that it is an outlier.

Figure 18 shows the scatter plot of both algorithms against the ground truth position of marker ID 34, where on it, it is possible to check the variance and bias of the data distributions more comprehensively in a zoomed-in scale by checking the confidence ellipses of three standard deviations. Again, the KMEA proved more reliable than the previous validated algorithm.

TABLE 3. **Part III - comparison of estimation metrics. The percentage change computation is of KMEA to LMEA.**

Metric	KMEA	LMEA	% Change
RMSE [m]	0.0075	0.0607	-87.6
STD [m]	0.0013	0.0011	14.0
MAE [m]	0.0073	0.0606	-88.0
MaxAE [m]	0.0105	0.0639	-84.0
MRE [%]	0.3496	2.9103	-88.0

The data presented in Table 3 summarizes the error metrics from Part III of the test, providing a more transparent analysis overview. This table demonstrates that KMEA outperforms

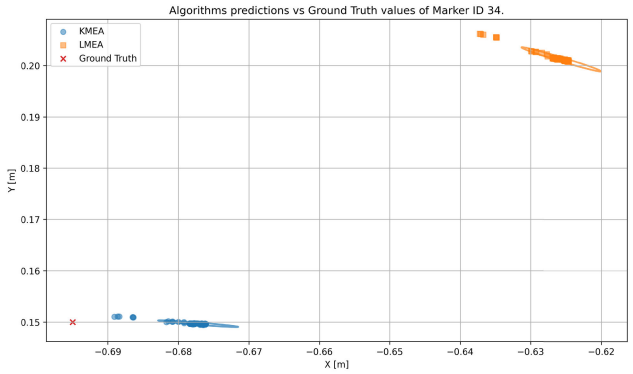

FIGURE 18. Part III - scatter plot of both algorithms and the ground truth position of marker ID 34.

LMEA in terms of robustness and accuracy. Despite the challenge of having three misaligned markers in the testbed, KMEA managed to keep its error metrics within a remarkably low range, under 1 cm and an MRE of 0.35%. In contrast, LMEA's performance significantly deteriorated, with errors averaging around 6 cm and an MRE of 2.9%. This is emphasized by analyzing KMEA's MAE, MaxAE, RMSE, and MRE values, which are consistently lower than LMEA. Both approaches showed stable and predictable performance with a high level of error consistency indicated by the similarity of the MaxAE regarding the metrics of RMSE and MAE, highlighting their ability to limit the maximum error to a level near its average errors.

The column labeled "% Change" in Table 3 is particularly revealing. It shows that, except for the STD, KMEA's error metrics are, on average, 86.9% lower than those of LMEA. This indicates a significant superiority in the accuracy, precision, and reliability of KMEA. The negligible difference in standard deviation between the two algorithms is consistent with previous observations and analyses discussed in this section.

D. PART IV. SEVERAL MARKERS ESTIMATED WITH ORTHONORMAL BASIS MARKERS DISTORTED, AND THE CAMERA'S POSE CHANGED

Part IV test had similar conditions as Part III with some changes. The main one was the camera's extrinsic parameters being changed. Since the algorithm does not need external calibration, the scenario change did not influence the results. In addition, the distortion of the orthonormal basis was much more substantial than in Part III, stressing both algorithms more. Finally, the set of the assessed markers was also changed. In this sense, Figure 19 shows the scatter plots of both algorithms against the evaluated markers' ground truth values.

As illustrated in Figures 19a and 19b, the dispersion of values were increased and also the bias relative to the true values was also heavily affected compared to previous tests. For a more thorough analysis, Figure 20 shows the five error metrics for the evaluated markers.

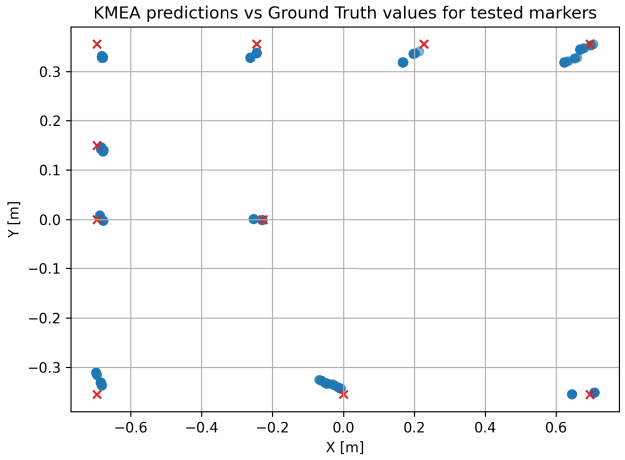

(a) Scatter plot of the markers' positions estimations of the KMEA against their ground truth values.

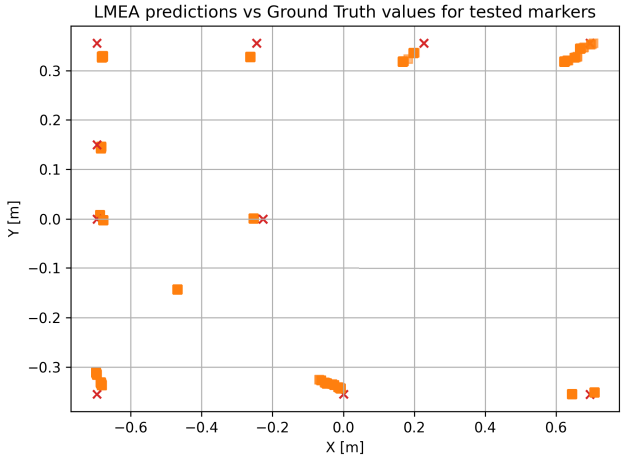

(b) Scatter plot of the markers' positions estimations of the LMEA against their ground truth values.

FIGURE 19. Part IV - comparative scatter plots of markers' position estimations by KMEA and LMEA.

The effect on the performance of the algorithms was more intense, evidenced by the displayed bar plots. Considering the MAE analysis in Figure 20a, the error ranged from 15 to 60 cm for the LMEA. On the other hand, the KMEA still managed to maintain acceptable levels, given the scenario's extreme conditions, with the MAE ranging from up to 5 cm of error. Analyzing Figure 20b, which displays the MaxAE error metrics, one can see that the maximum errors of LMEA reached absurd levels in the metric scale, indicating that the distortion made it useless in this scenario, whereas KMEA varied approximately in the range below of 10 cm. The results remained consistent in the other metrics, such as MRE, in Figure 20e, that LMEA errors ranged approximately from 3% to 30% and KMEA's errors all were below 2.5% which is an acceptable metric given the circumstances. In addition, the RMSE results, displayed in Figure 20c, showed absurd errors for LMEA, where KMEA still manages to have acceptable results in the centimetric scale. Finally, the STD metric, shown in Figure 20d, shows that in this

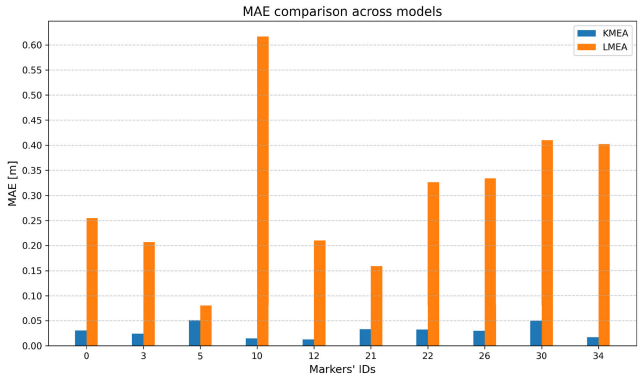

(a) Bar plot of MAE of both algorithms in the assessed markers.

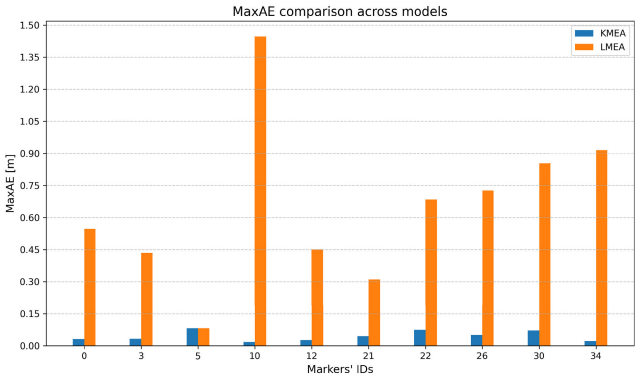

(b) Bar plot of MaxAE of both algorithms in the assessed markers.

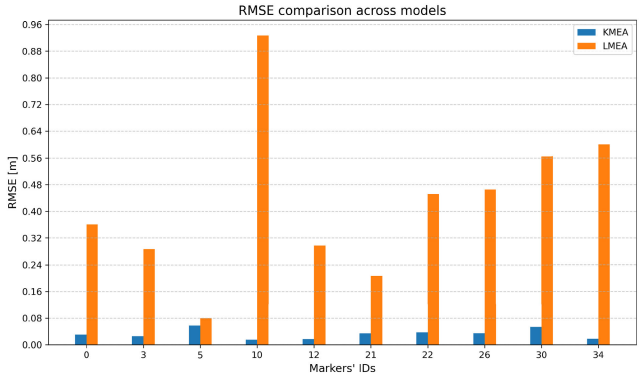

(c) Bar plot of RMSE of both algorithms in the assessed markers.

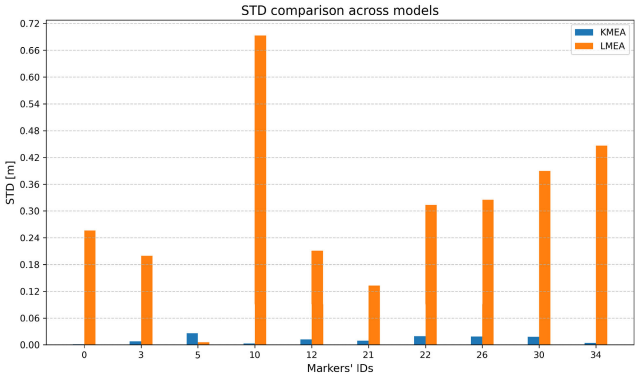

(d) Bar plot of STD of both algorithms in the assessed markers.

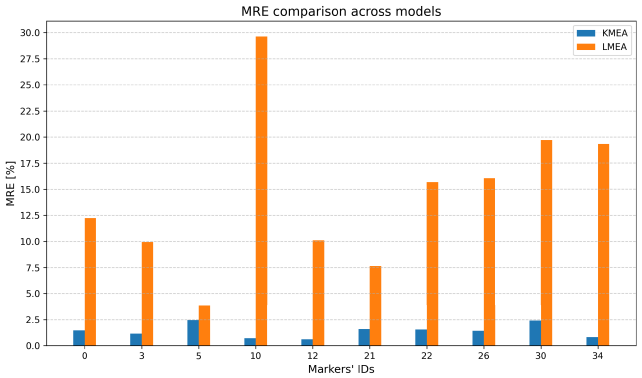

(e) Bar plot of MRE of both algorithms in the assessed markers.

FIGURE 20. **Part IV - bar plots of error metrics of both algorithms described in the test methodology.**

specific test, some markers were not consistently detected because of the camera's different pose and illumination. This caused LMEA to generate more dispersed estimations, increasing the STD metrics significantly with unacceptable values. KMEA, on the other hand, maintained its consistency in the acceptable, given the extreme scenario, centimetric scale.

Figure 21 shows a scatter plot of the ground truth position of tag five and estimations of both algorithms with confidence ellipses of three standard deviations. It is evident that scenario two provided worse conditions for both algorithms to perform, which increased their dispersion and bias in estimations. Table 4 displays the average of the error metrics across all evaluated markers and the percentage change of KMEA relative to LMEA.

TABLE 4. **Part IV - comparison of estimation metrics. The percentage change computation is of KMEA to LMEA.**

Metric	KMEA	LMEA	% Change
RMSE [m]	0.0322	0.4242	-92.4
STD [m]	0.0117	0.2972	-96.1
MAE [m]	0.0295	0.3000	-90.2
MaxAE [m]	0.0451	0.6451	-93.0
MRE [%]	1.4154	14.4180	-90.2

As described in Table 4, KMEA maintained acceptable metrics even in scenario two that provided absurd conditions.

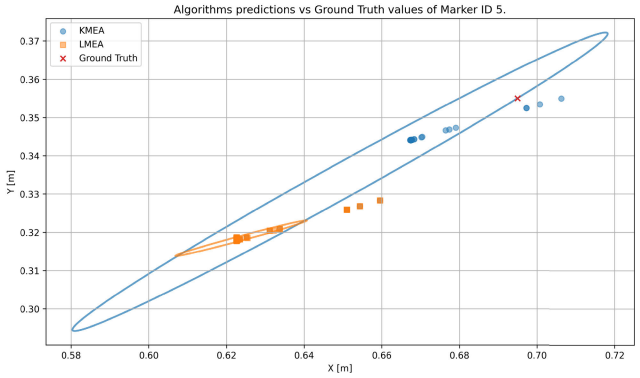

FIGURE 21. Part IV - scatter plot of both algorithms and the ground truth position of marker ID 5.

This is evidenced by average error metrics that ranged from 1 cm to 4.5 cm and a MRE of approximately 1.4%. LMEA, on the other hand, had worse results ranging from 30 cm to 64 cm and an MRE of approximately 14.4%. Finally, the ''% Change'' column shows an average of 92% reduction in the error metrics of KMEA relative to LMEA.

VI. CONCLUSION AND FUTURE WORK

This study presented the KMEA, a new marker-based localization algorithm that uses fiducial markers for pose estimation within a camera's FoV. Integrating the Kabsch Algorithm aligns detected markers with their ground truth positions, enhancing precision, robustness, and accuracy. This robustness is crucial in dynamic environments, such as industrial settings, where the movement of machinery and personnel can lead to marker damage or obstruction. The KMEA was evaluated in an I4.0 automated warehouse mockup, simulating the RAF competition environment. It outperformed the previous LMEA by using data from all visible markers rather than relying on a few select markers ; it also provides the independence of the camera's extrinsic parameters and less sensitivity to marker distortion. These features address the previous system's limitations, which depended on specific markers, and significantly improve robustness and adaptability in dynamic environments where marker visibility might be compromised. Despite the algorithms' sensitivity to camera calibration quality, the KMEA achieved comparable or superior accuracy to the LMEA in tests under normal conditions (tests one and two). This finding is notable, given the increased impact of radial distortion away from the image centre, since LMEA uses markers near the camera FoV's centre and KMEA uses all detected markers within a given frame. Furthermore, the KMEA proved robust even with marker misplacement and changing the camera extrinsic parameters. This was represented in Parts III and IV of the test methodology. KMEA maintained good accuracy and precision, whereas the LMEA's performance declined drastically to unacceptable levels in scale terms. This was corroborated by an average percentage decrease of the assessed metrics of 86.9% in the Part III test and 92% in the Part IV test of KMEA relative to LMEA. This research confirmed the potential of a marker-based localization system for indoor AMR localization within the I4.0 context. Its effectiveness, scalability, robustness, and broad applicability, extending to augmented reality and visual localization, make it a valuable asset in sectors requiring precise indoor localization.

Future work should focus on integrating outlier rejection algorithms and non-linear filtering techniques. Improving the pinhole camera model's distortions through non-linear optimization is also critical, as achieving perfect calibration is challenging.

REFERENCES

[1] G. Balamurugan, J. Valarmathi, and V. P. S. Naidu, ''Survey on UAV navigation in GPS denied environments,'' in *Proc. Int. Conf. Signal Process., Commun., Power Embedded Syst. (SCOPES)*, Oct. 2016, pp. 198–204.

[2] J. Braun, A. O. Junior, G. Berger, V. H. Pinto, I. N. Soares, A. I. Pereira, J. Lima, and P. Costa, ''A robot localization proposal for the RobotAtFactory 4.0: A novel robotics competition within the Industry 4.0 concept,'' *Frontiers Robot. AI*, vol. 9, pp. 1–15, Nov. 2022.

[3] R. M. Claro, D. B. Silva, and A. M. Pinto, ''ArTuga: A novel multimodal fiducial marker for aerial robotics,'' *Robot. Auto. Syst.*, vol. 163, May 2023, Art. no. 104398.

[4] P. García-Ruiz, R. Muñoz-Salinas, R. Medina-Carnicer, and M. J. Marín-Jiménez, ''Object localization with multiplanar fiducial markers: Accurate pose estimation,'' in *Proc. Iberian Conf. Pattern Recognit. Image Anal.*, 2023, pp. 454–465.

[5] F. Digiacomo, F. Bologna, F. Inglese, C. Stefanini, and M. Milazzo, ''MechaTag: A mechanical fiducial marker and the detection algorithm,'' *J. Intell. Robotic Syst.*, vol. 103, no. 3, pp. 1–14, Nov. 2021.

[6] M. Zhang, S. Han, X. Liu, S. Wang, L. Han, and J. Zhao, *Visual-Marker-Inertial Fusion Localization System Using Sliding Window Optimization*. Piscataway, NJ, USA: IEEE Press, 2021, pp. 3566–3572.

[7] G. Popovic, I. Cviic, I. Markovic, and I. Petrovic, *Human Localization in Warehouse Environments Based on a Wearable Camera Sensor Suite and Dynamic Ultra-Wide Band Nodes*. Piscataway, NJ, USA: IEEE Press, 2021, pp. 818–823.

[8] A. Alabbas, M. A. Cabrera, O. Alyounes, and D. Tsetserukou, *Arucoglide: A Novel Wearable Robot for Position Tracking and Haptic Feedback to Increase Safety During Human–Robot Interaction*. Piscataway, NJ, USA: IEEE Press, 2023, pp. 1–8.

[9] E. S. Kesuma, P. H. Rusmin, and D. A. Maharani, ''Pallet detection and distance estimation with YOLO and fiducial marker algorithm in industrial forklift robot,'' in *Proc. Int. Conf. Artif. Intell. Inf. Commun. (ICAIIC)*, Feb. 2023, pp. 270–275.

[10] C. Romero, C. Naufal, J. Meza, and A. Marrugo, ''A validation strategy for a target-based vision tracking system with an industrial robot,'' *J. Phys. Conf. Ser.*, vol. 1547, no. 1, 2020, Art. no. 012018.

[11] W. Zhang, L. Gong, Y. Sun, B. Gao, C. Yu, and C. Liu, ''Precise visual positioning of agricultural mobile robots with a fiducial marker reprojection approach,'' *Meas. Sci. Technol.*, vol. 34, no. 11, Nov. 2023, Art. no. 115110.

[12] J. Zhang, H. Zhang, X. Zhou, B. Chen, X. Wang, and T. Xu, ''A graph-based SLAM method assisted by visual marker in the degenerate scenes,'' in *Proc. Int. Conf. Adv. Robot. Mechatronics (ICARM)*, Jul. 2023, pp. 1–6.

[13] Q. Huang, J. DeGol, V. Fragoso, S. N. Sinha, and J. J. Leonard, ''Optimizing fiducial marker placement for improved visual localization,'' *IEEE Robot. Autom. Lett.*, vol. 8, no. 5, pp. 2756–2763, May 2023.

[14] M. Yang and E. Yang, ''Two-stage multi-sensor fusion positioning system with seamless switching for cooperative mobile robot and manipulator system,'' *Int. J. Intell. Robot. Appl.*, vol. 7, no. 2, pp. 275–290, Jun. 2023.

[15] R. Adámek, M. Brablc, P. Vávra, B. Dobossy, M. Formánek, and F. Radil, ''Analytical models for pose estimate variance of planar fiducial markers for mobile robot localisation,'' *Sensors*, vol. 23, no. 12, p. 5746, Jun. 2023.

[16] J. Huang, S. Junginger, H. Liu, and K. Thurow, ''Indoor positioning systems of mobile robots: A review,'' *Robotics*, vol. 12, no. 2, p. 47, Mar. 2023.

[17] D. Jurado-Rodriguez, R. Muñoz-Salinas, S. Garrido-Jurado, and R. Medina-Carnicer, "Planar fiducial markers: A comparative study," *Virtual Reality*, vol. 27, no. 3, pp. 1733–1749, Sep. 2023.
[18] L. C. Klein, J. Braun, J. Mendes, V. H. Pinto, F. N. Martins, A. S. de Oliveira, H. Wörtche, P. Costa, and J. Lima, "A machine learning approach to robot localization using fiducial markers in RobotAtFactory 4.0 competition," *Sensors*, vol. 23, no. 6, p. 3128, Mar. 2023.
[19] T. Kim, H. Jeon, and D. Lee, "A multi-layered 3D NDT scan-matching method for robust localization in logistics warehouse environments," *Sensors*, vol. 23, no. 5, p. 2671, Feb. 2023.
[20] M. Ekici, A. Ç. Seçkin, A. Özek, and C. Karpuz, "Warehouse drone: Indoor positioning and product counter with virtual fiducial markers," *Drones*, vol. 7, no. 1, p. 3, Dec. 2022.
[21] A. Kirsch, M. Riechmann, and M. Koenig, "Assisted localization of MAVs for navigation in indoor environments using fiducial markers," in *Proc. Eur. Conf. Mobile Robots (ECMR)*, Sep. 2023, pp. 1–17.
[22] J. Braun, A. O. Junior, G. S. Berger, J. Lima, A. I. Pereira, and P. Costa, "RobotAtFactory 4.0: A ROS framework for the SimTwo simulator," in *Proc. IEEE Int. Conf. Auto. Robot Syst. Competitions (ICARSC)*, Apr. 2022, pp. 205–210.
[23] J. Braun, K. Baidi, L. Bonzatto, G. Berger, M. Pinto, R. B. Kalbermatter, L. Klein, V. Grilo, A. I. Pereira, P. Costa, and J. Lima, "Design and development of an omnidirectional mecanum platform for the robotatfactory 4.0 competition," in *Proc. Climbing Walking Robots Conf.*, 2023, pp. 114–125.
[24] J. Lawrence, J. Bernal, and C. Witzgall, "A purely algebraic justification of the kabsch-umeyama algorithm," *J. Res. Nat. Inst. Standards Technol.*, vol. 124, p. 1, Oct. 2019.

JOÃO BRAUN received the double bachelor's degree in electronic engineering from the Federal Technological University of Paraná, Brazil, and the master's degree in industrial engineering from the Polytechnic Institute of Bragança, Portugal, in 2019. He is currently pursuing the Ph.D. degree in electrical and computer engineering with the University of Porto, Portugal, with a focus on robotics.

Currently, he is an Assistant Professor with the Polytechnic Institute of Bragança and a Researcher with CeDRI, Bragança, and INESC TEC—CRIIS, Porto. He has authored over 30 publications across journals, book chapters, and international conference proceedings. He has played significant roles in organizing and chairing sessions at international robotics and AI conferences and competitions, including chairing a major European robotics competition. He is actively involved in outreach activities, conducting workshops, supervising research projects, and contributing to educational initiatives. His work has received coverage in major Portuguese newspapers, highlighting his significant impact on robotics, engineering, and education.

Mr. Braun has been awarded three national robotics competition prizes and two doctoral scholarships: the Doctoral Fellowship INPhINIT by the "la Caixa" Foundation, in 2020, and the Doctoral Scholarship from the Foundation for Science and Technology (FCT), in 2024.

JOSÉ LIMA received the M.Sc. and Ph.D. degrees in electrical and computer engineering from the Faculty of Engineering, University of Porto, Portugal, in 2001 and 2009, respectively.

He joined the Polytechnic Institute of Bragança, in 2002, where he is currently pursuing a Coordinator Professor and the Head of the Electrical Engineering Department. He is also the Vice Coordinator of the Research Centre in Digitalization and Intelligent Robotics and a Researcher with the Centre for Robotics in Industry and Intelligent Systems, Institute for Systems and Computer Engineering, Technology and Science (INESC TEC), Porto, Portugal. He has published more than 200 papers in international scientific journals and conference proceedings and has developed various industrial applications. He has been actively involved in mobile robotics competitions, both as a participant and a juror, and has significantly contributed to the field through his research and supervision. He has participated in several national and international projects, supervised over 70 master's degree students, and is currently supervising eight Ph.D. students. His research interests include mobile robotics, simulation, and the Internet of Things (IoT).

ANA I. PEREIRA received the Ph.D. degree in numerical optimization from Minho University, in 2006.

She is currently a Coordinator Professor with the Department of Mathematics, Polytechnic Institute of Bragança, Portugal. She is also the Vice-Coordinator of the Research Centre in Digitalization and Intelligent Robotics (CeDRI), Polytechnic Institute of Bragança, and a Research Member with the Algorithm Research Centre, Minho University. Additionally, she holds a position as a Direction Member of Bragança "Ciência Viva" Science Centre. She has authored or coauthored over 120 journal articles, book chapters, and conference proceedings. She has been actively involved in more than 20 research projects. Her contributions to academia and research have been marked by her involvement in numerous projects and publications. She has played a significant role in advancing research in her fields of expertise, particularly in developing innovative approaches in teaching and research in robotics and optimization. Her research interests include robotics, optimization, and innovative tools in teaching.

PAULO COSTA received the M.Sc. and Ph.D. degrees in electrical and computer engineering from the Faculty of Engineering, University of Porto, Portugal, in 1995 and 2000, respectively.

He began his career with the Faculty of Engineering, University of Porto, in 1992, where has been a Professor with the Electrical Engineering Department, since 1992. He is currently a Senior Researcher with the Centre for Robotics in Industry and Intelligent Systems, Institute for Systems and Computer Engineering, Technology and Science (INESC TEC), Porto, Portugal). He has published more than 100 papers in international scientific journals and conference proceedings and has been an active participant in many AMR competitions. He has been involved in various national and international projects, including H2020-funded projects, like PRODUTECH SIF, ScalABLE4.0, CARLOS, and PNEUMA. His contributions to the field of robotics and automation have been significant, particularly in the development and application of advanced technologies in mobile robotics. His research interests include robotics and automation, focusing on simulation, path planning, artificial vision, mobile robot localization and navigation, obstacle avoidance, and perception.